Short communication

CONTRAST MEDIA & MOLECULAR IMAGING

Received: 10 January 2016, Revised: 27 April 2016, Accepted: 2 May 2016, Published online in Wiley Online Library: 16 June 2016

(wileyonlinelibrary.com) DOI: 10.1002/cmmi.1699

A theoretical analysis of chemical exchange saturation transfer echo planar imaging (CEST-EPI) steady state solution and the CEST sensitivity efficiency-based optimization approach

Weiping Jiang[a,b], Iris Yuwen Zhou[a], Lingyi Wen[a], Xin Zhou[b]* and Phillip Zhe Sun[a,c]*

Chemical exchange saturation transfer (CEST) MRI is sensitive to dilute labile protons and microenvironmental properties, augmenting routine relaxation-based MRI. Recent developments of quantitative CEST (qCEST) analysis such as omega plots and RF-power based ratiometric calculation have extended our ability to elucidate the underlying CEST system beyond the simplistic apparent CEST measurement. CEST MRI strongly varies with experimental factors, including the RF irradiation level and duration as well as repetition time and flip angle. In addition, the CEST MRI effect is typically small, and experimental optimization strategies have to be carefully evaluated in order to enhance the CEST imaging sensitivity. Although routine CEST MRI has been optimized largely based on maximizing the magnitude of the CEST effect, the CEST signal-to-noise (SNR) efficiency provides a more suitable optimization index, particularly when the scan time is constrained. Herein, we derive an analytical solution of the CEST effect that takes into account key experimental parameters including repetition time, imaging flip angle and RF irradiation level, and solve its SNR efficiency. The solution expedites CEST imaging sensitivity calculation, substantially faster than the Bloch–McConnell equation-based numerical simulation approach. In addition, the analytical solution-based SNR formula enables the exhaustive optimization of CEST MRI, which simultaneously predicts multiple optimal parameters such as repetition time, flip angle and RF saturation level based on the chemical shift and exchange rate. The sensitivity efficiency-based optimization approach could simplify and guide imaging of CEST agents, including glycogen, glucose, creatine, gamma-aminobutyric acid and glutamate.

Keywords: chemical exchange saturation transfer (CEST); contrast-to-noise ratio (CNR); quantitative CEST (qCEST); signal-to-noise ratio (SNR); specific absorption rate (SAR)

1. INTRODUCTION

Chemical exchange saturation transfer (CEST) MRI is sensitive to the chemical exchange process between labile protons and bulk water signal, providing a contrast mechanism for imaging dilute CEST agents and microenvironment properties such as pH and temperature (1–5). Indeed, CEST-weighted MRI has found substantial interest in molecular imaging as well as *in vivo* applications such as acute stroke (6–15), tumor (16–24) and epilepsy imaging (25). Whereas the CEST MRI measurement varies with experimental factors, particularly the RF irradiation level and duration, such dependence has been harnessed as a novel approach for quantitative CEST (qCEST) analysis, including omega plots and RF-power based ratiometric calculation (26–33). It is necessary to point out that the development of qCEST analysis allows simultaneous determination of the CEST agent concentration and exchange rate with minimal *a priori* information, advancing CEST MRI as a novel molecular imaging approach (34–37).

Despite the substantial sensitivity advantage of CEST imaging over MR spectroscopy, the CEST MRI effect is typically small due to the relatively low concentration and/or moderate exchange rate, requiring meticulous optimization (38–45). It has been shown that the apparent CEST MRI measurement

* *Correspondence to: X. Zhou, State Key Laboratory of Magnetic Resonance and Atomic and Molecular Physics, National Center for Magnetic Resonance in Wuhan, Wuhan Institute of Physics and Mathematics, Chinese Academy of Sciences Wuhan, China. Email: xinzhou@wipm.ac.cn*
P. Z. Sun, Athinoula A. Martinos Center for Biomedical Imaging, Department of Radiology, Massachusetts General Hospital and Harvard Medical School, Charlestown, MA, USA. Email: pzhesun@mgh.harvard.edu

a *W. Jiang, I. Y. Zhou, L. Wen, P. Z. Sun*
Athinoula A. Martinos Center for Biomedical Imaging, Department of Radiology, Massachusetts General Hospital and Harvard Medical School, Charlestown, MA, USA

b *W. Jiang, X. Zhou*
State Key Laboratory of Magnetic Resonance and Atomic and Molecular Physics, National Center for Magnetic Resonance in Wuhan, Wuhan Institute of Physics and Mathematics, Chinese Academy of Sciences, Wuhan, China

c *P. Z. Sun*
Department of Radiology, University of Illinois at Chicago, IL, USA

strongly varies with the RF irradiation level (B_1) and duration. Recent studies have also shown that the CEST effect depends on experimental factors such as repetition time (*TR*) and flip angle (FA), which need to be taken into account for proper optimization (46). Although CEST optimization strategies have been largely based on maximization of the CEST effect, the CEST signal-to-noise (SNR) per unit time (efficiency)-based optimization approach ensures the maximal CEST MRI sensitivity, particularly important when the total scan time is constrained (47,48). Because the fully relaxed magnetization state under an extremely long repetition time is rarely used, we here derived a steady state analytical solution for the CEST MRI effect, and solved its SNR efficiency as a function of experimental variables including *TR* and FA. We confirmed that the analytical solution provides accurate quantification of the CEST MRI effect, in good agreement with Bloch–McConnell equation-based numerical simulation. In addition, the use of the analytical solution accelerates SNR efficiency computation, enabling the exhaustive optimization approach to simultaneously optimize multiple parameters, which could simplify and guide experimental optimization.

2. THEORY

2.1. Quantitative solution of CEST MRI effect

For the representative CEST echo planar imaging (EPI) sequence with a continuous wave (CW) RF saturation (Fig. 1), the control scan signal without RF irradiation can be shown to be (49)

$$S_0(TR,\mathrm{FA}) = \frac{1-\mathrm{e}^{-TR/T_{1w}}}{1-\cos(\mathrm{FA})\mathrm{e}^{-TR/T_{1w}}}\sin(\mathrm{FA})\mathrm{e}^{-TE/T^*_{2w}} \quad (1)$$

where *TR* is the repetition time, *TE* is the echo time, T_{1w} and T^*_{2w} are the bulk water longitudinal and apparent transverse relaxation times, respectively, and FA is the image excitation flip angle. For the irradiated scans, the steady state signal (see Appendix A.1) can be solved as (36,50–52)

Note that we assumed short EPI readout time (i.e., $TR = T_r + T_s$, where T_r and T_s are the relaxation recovery and saturation times, respectively). We have $R_{1\rho} = R_{1w}\cos^2\theta + \left(R_{2w} + \frac{f_s k_{sw}\alpha}{(\omega_1/\delta_s)^2+(k_{sw}/\delta_s)^2}\right)\sin^2\theta$, where $R_{1,2w}$ are the bulk water longitudinal and transverse relaxation rates, δ_s is the labile proton offset and α is the saturation coefficient $\alpha = \frac{\omega_1^2}{pq+\omega_1^2}$, in which $p = r_{2s} - \frac{k_{sw}k_{ws}}{r_{2w}}$, $q = r_{1s} - \frac{k_{sw}k_{ws}}{r_{1w}}$, $k_{ws} = f_s k_{sw}$ and $r_{1w,s;2w,s} = R_{1w,s;2w,s} + k_{ws,sw;2w,s}$. In addition, we have $\theta = \tan^{-1}(\omega_1/\Delta\omega)$, where ω_1 and $\Delta\omega$ are the RF irradiation level and offset, f_s and k_{sw} are the labile proton ratio and exchange rate, and $R_{1s,2s}$ are their longitudinal and transverse relaxation rates, respectively. The CEST MRI signal is given as (see Appendix A.1)

$$\frac{S_{sat}(R_{1\rho},TR,\mathrm{FA},T_s,B_1)}{S_0(TR,\mathrm{FA})} = \frac{\frac{\left(1-\mathrm{e}^{-T_r/T_{1w}}\right)\mathrm{e}^{-R_{1\rho}T_s}+\frac{R_{1w}\cos^2\theta}{R_{1\rho}}\left(1-\mathrm{e}^{-R_{1\rho}T_s}\right)}{1-\cos(\mathrm{FA})\mathrm{e}^{-T_r/T_{1w}}\mathrm{e}^{-R_{1\rho}T_s}}}{\left(1-\mathrm{e}^{-TR/T_{1w}}\right)/\left(1-\cos(\mathrm{FA})\mathrm{e}^{-TR/T_{1w}}\right)}. \quad (3)$$

2.2. Quantitative CEST indices

The routinely used CEST asymmetry ratio (CESTR) is given as $\mathrm{CESTR} = \frac{S_{ref}-S_{lab}}{S_0}$, where S_{ref} and S_{lab} are scans with RF saturation applied at the labile proton frequency and reference offset, respectively, and S_0 is the control scan without RF saturation. Note that CESTR is complex, being a function of labile proton concentration, exchange rate and chemical shift as well as relaxation times and experimental factors such as *TR*, FA, T_s and B_1. It is necessary to point out that the inverse CEST asymmetry ratio, $\mathrm{CESTR}_{ind} = \frac{S_0}{S_{lab}} - \frac{S_0}{S_{ref}}$, is related to the conventional CESTR: $\mathrm{CESTR}_{ind} = \left(\frac{S_0^2}{S_{lab}S_{ref}}\right)\mathrm{CESTR}$ (53).

2.3. CEST SNR and CNR efficiency

It has been shown that the SNR for the routine CEST analysis (CESTR) is given by (46)

$$S_{sat}(R_{1\rho},TR,\mathrm{FA},T_s,B_1) = \frac{\left(1-\mathrm{e}^{-T_r/T_{1w}}\right)\mathrm{e}^{-R_{1\rho}T_s}+\frac{R_{1w}\cos^2\theta}{R_{1\rho}}\left(1-\mathrm{e}^{-R_{1\rho}T_s}\right)}{1-\cos(\mathrm{FA})\mathrm{e}^{-T_r/T_{1w}}\mathrm{e}^{-R_{1\rho}T_s}}\sin(\mathrm{FA})\mathrm{e}^{-TE/T^*_{2w}}. \quad (2)$$

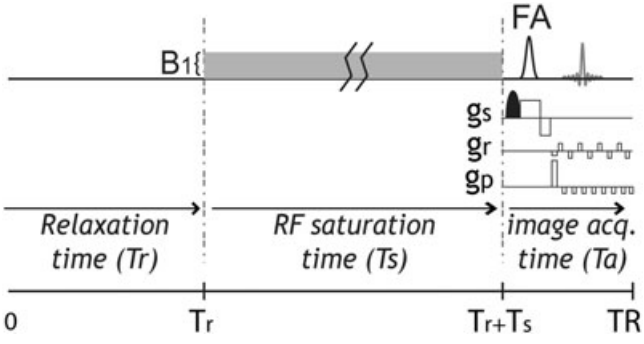

Figure 1. Illustration of CEST EPI pulse sequence that includes relaxation delay and RF saturation time (T_s) under an RF field denoted by B_1. Because the EPI duration is substantially shorter than typical T_r and T_s, which are of the order of T_{1w}, the repetition time is approximately equal to the sum of T_r and T_s.

$$\mathrm{SNR}_{\mathrm{CESTR}}(f_s,k_{sw},TR,\mathrm{FA},T_s,B_1) \approx \frac{\mathrm{CESTR}}{\sqrt{2+\mathrm{CESTR}^2}}\mathrm{SNR}_{S_0(TR,\mathrm{FA})} \quad (4a)$$

where SNR_{S_0} is the SNR of the control image, which depends on *TR* and FA. The SNR for CESTR_{ind} can be shown to be (see Appendix A.2)

$$\mathrm{SNR}_{\mathrm{CESTR}_{ind}}(f_s,k_{sw},TR,\mathrm{FA},T_s,B_1) = \frac{\mathrm{CESTR}}{\sqrt{2+\mathrm{CESTR}^2\left(1+\left(\frac{S_0}{S_{ref}}+\frac{S_0}{S_{lab}}\right)^2\right)}}\mathrm{SNR}_{S_0(TR,\mathrm{FA})}. \quad (4b)$$

For small CEST effect, we have $\mathrm{CESTR}^2 \ll 1$, and the SNRs for CESTR and CESTR_{ind} are approximately equal. The SNR per unit time (SNR efficiency) can be calculated from the SNR with

normalization by the square root of the total scan time (i.e. $SNR_{put} = SNR/\sqrt{scan\ time}$). Notably, the relative SNR (rSNR) is calculated by normalizing the CEST SNR by the SNR of the thermal equilibrium signal to have a uniform reference.

$$\mathrm{rSNR} = \frac{\mathrm{SNR}_{\mathrm{CESTR}_{\mathrm{ind}}}(f_s, k_{sw}, TR, \mathrm{FA}, T_s, B_1)}{\mathrm{SNR}_{S_0(TR=\infty,\mathrm{FA}=\pi/2)}}. \quad (5)$$

The CEST effect CNR can be derived following the error propagation theorem. For the routine CESTR calculation, we have (see Appendix A.3)

$$\mathrm{CNR} = \frac{|\mathrm{CESTR}(f_a, \mathrm{pH}_a\ldots) - \mathrm{CESTR}(f_b, \mathrm{pH}_b\ldots)|}{\sqrt{\begin{matrix}(\mathrm{CESTR}(f_a, \mathrm{pH}_a\ldots)\mathrm{SNR}_{\mathrm{CESTR}(f_b,\mathrm{pH}_b\ldots)})^2 \\ +(\mathrm{CESTR}(f_b, \mathrm{pH}_b\ldots)\mathrm{SNR}_{\mathrm{CESTR}(f_a,\mathrm{pH}_a\ldots)})^2\end{matrix}}} \mathrm{SNR}_{\mathrm{CESTR}(f_a,\mathrm{pH}_a\ldots)}\mathrm{SNR}_{\mathrm{CESTR}(f_b,\mathrm{pH}_b\ldots)} \quad (6)$$

where subscripts a and b denote different labile proton ratios and/or exchange rates. This shows that the CNR can be derived based on the SNR and CEST effects calculated from the analytical solution. Similarly, the CNR efficiency can be calculated from the CNR with normalization by the square root of the scan time. Note that Equation (6) is general and can be applied to alternative CEST indices.

3. RESULTS AND DISCUSSION

Figure 1 illustrates a CEST gradient echo EPI sequence with a continuous wave (CW) RF irradiation. Because the typical EPI echo time is negligible compared with *TR* and saturation time, TR is approximately equal to the sum of the relaxation recovery duration and saturation time (i.e., $TR \approx T_r + T_s$). The RF duty cycle is given by T_s/TR, which we set to 50% for typical RF amplifier performance. The steady state CEST solution was derived following the spin locking theorem (50,54) and relaxation recovery (see Appendix A.1).

Figure 2 tests the accuracy of the analytical CEST solution (Eq. (3)) against the Bloch–McConnell equation-based numerical simulation, assuming representative parameters of $T_{1w} = 2$ s, $T_{1s} = 1$ s, $T_{2w} = 100$ ms and $T_{2s} = 15$ ms. We assumed a typical labile proton ratio and exchange rate of 1:1000 and 100 s^{-1} at a representative chemical shift of 2 ppm at 4.7 T. Figure 2(a) shows three *Z*-spectra from −3 to 3 ppm for representative *TR* values of 1, 2 and 5 times T_{1w}. For simplicity, we assumed an FA of 90°. Note that the normalized signal intensity decreases with *TR* due to inadequate relaxation recovery. Figure 2(b) shows the CESTR estimated from the steady state non-equilibrium solution. Notably, CESTR decreases at short *TR* due to reduced saturation duration. Figure 2(c) compares rSNR efficiency calculated from the analytical solution with that simulated from Bloch–McConnell equations. Briefly, we used the randn function in MATLAB to generate normally distributed pseudorandom numbers, which were superimposed on simulated control, reference and label signals, and calculated the

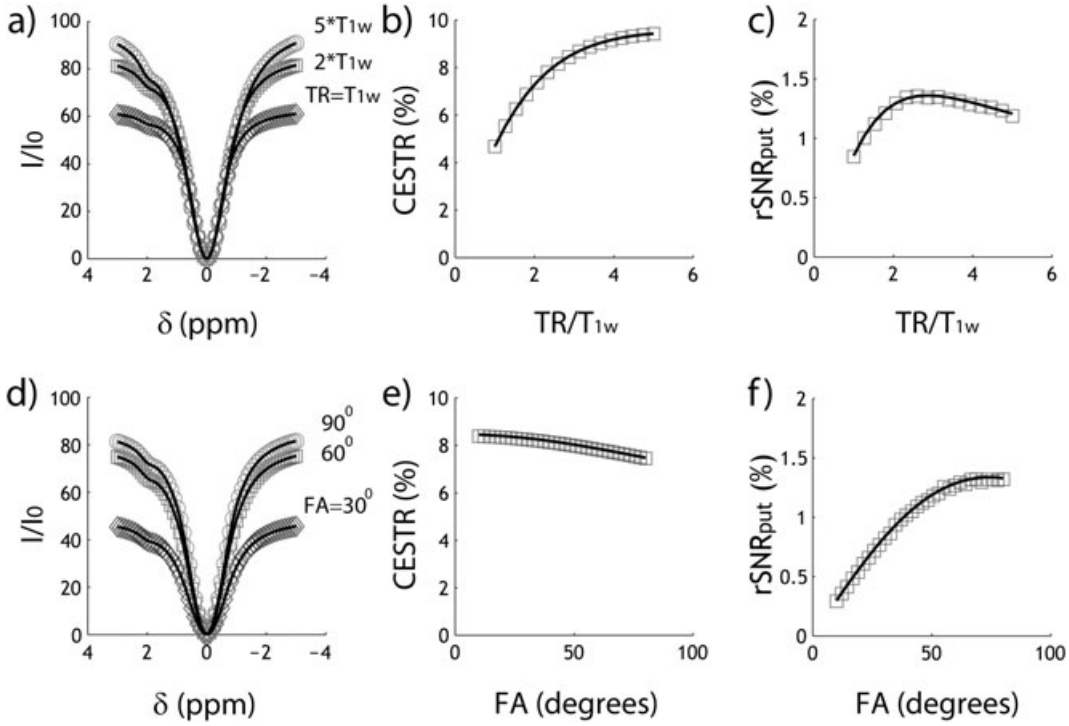

Figure 2. Evaluation of the steady state CEST analytical solution. Markers are data points simulated from Bloch–McConnell equations while lines are from the analytical solution. (a) *Z*-spectra for three representative *TR* values of 1, 2 and 5 times T_{1w}. (b) CESTR as a function of *TR*. (c) CEST rSNR efficiency as a function of *TR*. (d) *Z*-spectra for three representative FAs of 30, 60 and 90°. (e) CESTR as a function of FA. (f) CEST rSNR efficiency as a function of FA.

CESTR. The noise superimposition was repeated 8192 times to estimate SNR. Admittedly, it took 35 s to numerically solve the SNR (Dell Precision T7400, 8 GB RAM, E5420 dual processors), while the computation time was less than 0.01 s using the analytical solution, equivalent to an acceleration factor of over 3500. This advantage enables the practical use of the exhaustive optimization strategy for designing the CEST MRI experiment. Figure 2(d) shows three *Z*-spectra for representative flip angles of 30, 60 and 90°, assuming a typical *TR* of twice T_{1w}. The analytical solution and numerical simulation are in good agreement. The apparent CEST effect decreases with FA (Fig. 2(e)), consistent with prior findings (46). Figure 2(f) shows that rSNR efficiency peaks at an FA of approximately 75°. Note that the optimal FA for maximal CEST imaging rSNR is different from the Ernst angle, being 82° for $TR = 2T_{1w}$.

Figure 3 compares CESTR and $CESTR_{ind}$ effects and their sensitivities. We assumed a relatively optimal *TR* of 4 s (i.e. ~$2T_{1w}$) and FA of 75° (Fig. 2). Figure 3(a) shows that $CESTR_{ind}$ is consistently higher than CESTR, particularly for strong B_1. This is because $CESTR_{ind}$ is not sensitive to the direct RF spillover effect. Interestingly, Figure 3(b) shows that the SNR efficiency for routine CESTR analysis is approximately equal to but marginally higher than that of $CESTR_{ind}$. This is consistent with Equation (4b), which shows that, for small CEST effect, CESTR and $CESTR_{ind}$ analyses provide approximately the same CEST imaging sensitivity.

Figure 4 demonstrates the steady state solution-based exhaustive optimization strategy. Figure 4(a) shows the peak rSNR efficiency as a function of exchange rate and labile proton chemical shift under simultaneously optimized *TR*, B_1 and FA. Because the effective longitudinal relaxation rate for label scan (i.e. $R_{1\rho}^{+}$) increases with the exchange rate, the optimal *TR* (TR_{opt}) decreases at high exchange rate (Fig. 4(b)). Interestingly, TR_{opt} decreases at small chemical shift, likely because a moderate *TR* results in an enhancement of the apparent concentration of labile protons, as the labile proton signal typically relaxes faster than bulk water. Figure 4(c) shows that the optimal B_1 increases with both the exchange rate and chemical shift, as expected. Figure 4(d) shows that the optimal FA decreases at small chemical shift and high exchange rate, likely due to the decreased optimal *TR* under such conditions. It has been shown that under the conditions of near bulk water resonance and large B_1 field there could be an oscillatory signal due to the residual transverse magnetization (52). Because the typical saturation duration is significantly longer than the transverse relaxation time in the rotating frame (i.e. $T_{2\rho}$), the oscillatory signal should be small, warranting Equation (2). Because of its advantage to simultaneously optimize *TR*, FA and B_1, Figure 5(a) shows that the exhaustive optimization strategy identifies peak SNR efficiency substantially higher than that assuming the thermal equilibrium state (i.e., $TR = 5T_{1w}$). This is because CEST MRI experimental variables have relatively complex interdependence, and the exhaustive optimization approach faithfully optimizes multiple variables concurrently. Indeed, the optimal B_1 level determined from the exhaustive optimization strategy is substantially higher than the routine prediction based on the long *TR* solution (Fig. 5(b)). We further applied the CEST sensitivity efficiency-based optimization strategy and predicted optimal *TR*, FA and B_1 for a number of representative CEST agents at 4.7 T, including Gly (55), Glc (50), Cr (56), GABA (55), Glu (16) and ensemble amides (6), based on their exchange rates and chemical shifts (Table 1).

Our study derived the steady state non-thermal-equilibrium CEST solution and its sensitivity efficiency. The substantial acceleration in computation speed over the conventional Bloch–McConnell numerical approach enables prediction of optimal values for multiple parameters, which could simply guide CEST MRI experimental optimization (57–60). It complements the conventional optimization strategy that assumes the thermal equilibrium state, which is rarely implemented experimentally. By incorporating experimental factors such as *TR* and FA into the solution, our work is promising to improve the accuracy of qCEST analysis (36). Although our study here investigates only continuous wave (CW)-CEST MRI with GE EPI readout, the results may be generalized to several other commonly used image sequences. For example, adding a flip-back RF pulse after the readout in spin echo EPI resets the *Z*-magnetization similarly to GE EPI readout, provided that there is negligible spin relaxation during the echo time (i.e., $TE \ll T_{1w}$), and therefore the formulas derived in our study are applicable. For the case of rapid acquisition with relaxation enhancement (RARE) readout, if no *Z*-magnetization is recycled to the next scan, the spin relaxes towards its equilibrium state from null, similar to the spin evolution for a GE EPI readout with a 90° excitation pulse. It is necessary to point out that the formula can also be extended to include the contribution from magnetization transfer (MT) and/or multiple exchangeable sites by modifying the relaxation rate term (40). However, MT properties vary a lot in different tissues from blood to brain to kidney (61). Because the complexity of the SNR calculation increases exponentially with the number of dimensions, it is suggested to

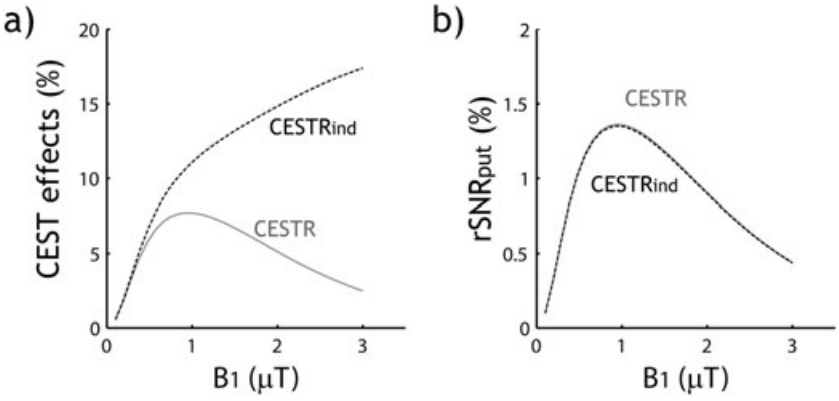

Figure 3. Comparison of the magnitudes of the CEST effect and their sensitivities measured by CESTR and $CESTR_{ind}$. (a) Routine CEST asymmetry analysis (CESTR) and the direct RF saturation-compensated inverse CEST asymmetry ($CESTR_{ind}$) as a function of B_1. (b) SNR efficiency of CESTR and $CESTR_{ind}$ as a function of B_1.

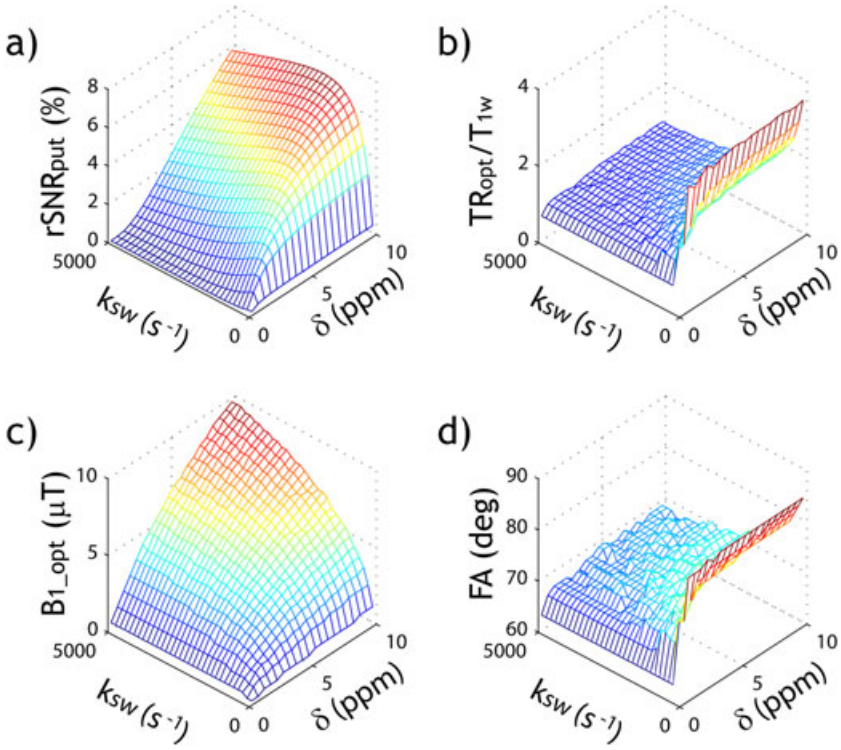

Figure 4. Evaluation of the exhaustive optimization strategy of CEST MRI. (a) Peak SNR efficiency as a function of labile proton exchange rate and chemical shift. (b) Optimal *TR* normalized by T_{1w} as a function of labile proton exchange rate and chemical shift. (c) Optimal B_1 as a function of labile proton exchange rate and chemical shift. (d) Optimal FA as a function of labile proton exchange rate and chemical shift.

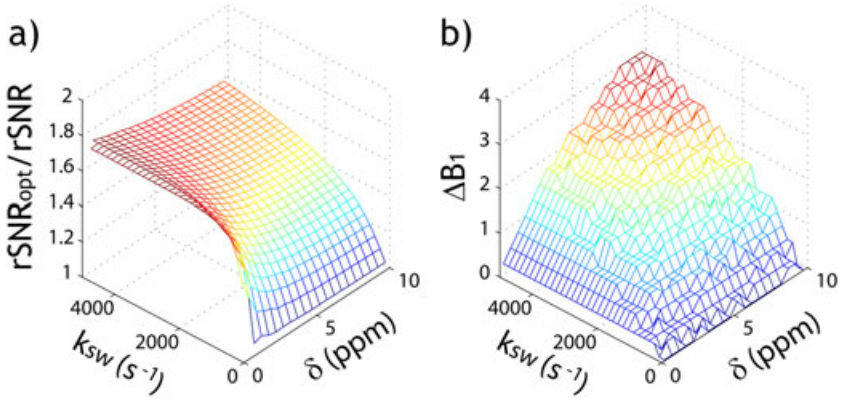

Figure 5. Demonstration of the advantage of the exhaustive optimization strategy. (a) Ratio of peak SNR efficiency from the exhaustive optimization strategy (*TR*, FA and B_1 optimization) over that assuming a long *TR*. (b) The optimal B_1 difference between the exhaustive optimization strategy and routine optimization approach assuming a long *TR*.

Table 1. Suggested experimental parameters from SNR efficiency-based optimization algorithm for representative metabolites at 4.7 T

	δ_s (ppm)	k_{sw} (s^{-1})	TR_{opt}/T_{1w}	FA_{opt} (°)	B_{1_opt} (μT)
Glc	~1.1	~4680 (pH = 7.4, rm temp.)	0.9	67	2.0
Gly	~1.2	~600 (pH = 7.4, 25 °C)	1.3	72	1.5
Cr	1.9	~1190 (pH = 7.0, 37 °C)	1.2	71	2.3
GABA	2.8	~800 (pH = 5.6, 25 °C)	1.6	75	2.5
Glu	3.0	~5500 (pH = 7.0, 37 °C)	0.9	68	4.3
Amides	~3.5	~30 (pH = 7.0, 37 °C)	3.4	85	0.8

first determine non-adjustable parameters such as relaxation, magnetic field strength and MT, and treat them as fixed variables in order to expedite the sensitivity efficiency-based optimization prediction.

Our study here showed that the inverse CEST asymmetry provides nearly identical SNR to the routine asymmetry analysis, despite the difference in their magnitudes. This finding helps to clarify the advantage and limitation of different means of CEST quantification. The derivation of SNR and CNR efficiency can be extended to alternative means of qCEST analysis. For example, the SNR of the recently proposed RF power-based ratiometric analysis (i.e. PRCESTR and PRICESTR) can be directly estimated from the SNR of CESTR and $CESTR_{ind}$ (see Appendix A.3). It is worth noting that the analytical solution also allows constrained optimization. For instance, the specific absorption rate (SAR) limit can be included in the SNR efficiency optimization computation by restricting the magnitude and duration of RF saturation ($SAR \propto \int_0^{T_s} B_1^2 dt/TR$) while searching for the optimal experimental conditions under the constraint. Our work here only investigated the CW RF irradiation scheme. For labile protons undergoing slow chemical exchange, it has been shown that the pulsed RF irradiation provides a similar CEST effect to CW irradiation (62,63). In addition, the recent derivation of an approximate solution for the pulsed CEST MRI effect (64) may be incorporated into the sensitivity solution to further refine optimization of the pulsed CEST MRI scheme.

4. CONCLUSIONS

Our study derives the steady state non-thermal equilibrium analytical solution of CEST imaging, its SNR and CNR efficiency, providing an expeditious and quantitative description of the CEST MRI sensitivity. The solution elucidates the effects of key scan parameters on CEST MRI measurements, thereby facilitating the use of an exhaustive optimization strategy to simultaneously optimize multiple parameters and enhance the sensitivity of CEST MRI.

5. MATERIALS AND METHODS

The CEST MRI effect was simulated using Bloch–McConnell equations of a typical two-pool exchange model in MATLAB (MathWorks, Natick, MA, USA), assuming representative bulk water T_{1w} and T_{2w} of 2 s and 100 ms, and T_{1s} and T_{2s} of 1 s and 15 ms, respectively (65). To test the accuracy of the non-equilibrium steady state analytical solution, we simulated a typical labile proton ratio and exchange rate of 1:1000 and $100\,s^{-1}$ for a representative chemical shift of 2 ppm at 4.7 T. The SNR was calculated using Equation (4a) and compared with the numerically simulated SNR from Bloch–McConnell equations, as described previously (46). To evaluate the optimal experimental conditions for CEST MRI, we calculated the multi-dimensional SNR efficiency for each set of *TR*, FA and B_1, with *TR* from 0.5 to 10 s with intervals of 0.1 s, FA from 60° to 90° with intervals of 1° and B_1 from 0 to 10 μT with intervals of 0.25 μT. In addition, we investigated broad ranges of exchange rate and chemical shift from 25 to $5500\,s^{-1}$ with intervals of $87\,s^{-1}$, and from 0.5 to 10 ppm with intervals of 0.25 ppm, respectively.

Acknowledgments

This study was supported in part by grants from the National Natural Science Foundation of China, NSFC81227902 (Zhou), and the National Institutes of Health, 1R01NS083654 (Sun) and 1U01HD087211 (Grant/Adalsteinsson/Wald).

REFERENCES

1. Ward KM, Balaban RS. Determination of pH using water protons and chemical exchange dependent saturation transfer (CEST). Magn Reson Med 2000; 44(5): 799–802.
2. Terreno E, Castelli DD, Viale A, Aime S. Challenges for molecular magnetic resonance imaging. Chem Rev 2010; 110(5): 3019–3042.
3. van Zijl PCM, Yadav NN. Chemical exchange saturation transfer (CEST): what is in a name and what isn't? Magn Reson Med 2011; 65(4): 927–948.
4. Vinogradov E, Sherry AD, Lenkinski RE. CEST: from basic principles to applications, challenges and opportunities. J Magn Reson 2013; 229 (0): 155–172.
5. Huang Y, Coman D, Ali MM, Hyder F. Lanthanide ion (III) complexes of 1,4,7,10-tetraazacyclododecane-1,4,7,10-tetraaminophosphonate for dual biosensing of pH with chemical exchange saturation transfer (CEST) and biosensor imaging of redundant deviation in shifts (BIRDS). Contrast Media Mol Imaging 2015; 10(1): 51–58.
6. Zhou J, Payen JF, Wilson DA, Traystman RJ, van Zijl PC. Using the amide proton signals of intracellular proteins and peptides to detect pH effects in MRI. Nat Med 2003; 9(8): 1085–1090.
7. Sun PZ, Zhou J, Sun W, Huang J, van Zijl PC. Detection of the ischemic penumbra using pH-weighted MRI. J Cereb Blood Flow Metab 2007; 27(6): 1129–1136.
8. Zhou J, Tryggestad E, Wen Z, Lal B, Zhou T, Grossman R, Wang S, Yan K, Fu D-X, Ford E, Tyler B, Blakeley J, Laterra J, van Zijl PCM. Differentiation between glioma and radiation necrosis using molecular magnetic resonance imaging of endogenous proteins and peptides. Nat Med 2011; 17(1): 130–134.
9. Sun PZ, Cheung JS, Wang EF, Lo EH. Association between pH-weighted endogenous amide proton chemical exchange saturation transfer MRI and tissue lactic acidosis during acute ischemic stroke. J Cereb Blood Flow Metab 2011; 31(8): 1743–1750.
10. Sun PZ, Wang E, Cheung JS. Imaging acute ischemic tissue acidosis with pH-sensitive endogenous amide proton transfer (APT) MRI – correction of tissue relaxation and concomitant RF irradiation effects toward mapping quantitative cerebral tissue pH. Neuroimage 2012; 60(1): 1–6.
11. Zong X, Wang P, Kim S-G, Jin T. Sensitivity and source of amine-proton exchange and amide-proton transfer magnetic resonance imaging in cerebral ischemia. Magn Reson Med 2014; 71(1): 118–132.
12. McVicar N, Li AX, Goncalves DF, Bellyou M, Meakin SO, Prado MAM, Bartha R. Quantitative tissue pH measurement during cerebral ischemia using amine and amide concentration-independent detection (AACID) with MRI. J Cereb Blood Flow Metab 2014; 34(4): 690–698.
13. Tietze A, Blicher J, Mikkelsen IK, Østergaard L, Strother MK, Smith SA, Donahue MJ. Assessment of ischemic penumbra in patients with hyperacute stroke using amide proton transfer (APT) chemical exchange saturation transfer (CEST) MRI. NMR Biomed 2014; 27(2): 163–174.
14. Harston GWJ, Tee YK, Blockley N, Okell TW, Thandeswaran S, Shaya G, Sheerin F, Cellerini M, Payne S, Jezzard P, Chappell M, Kennedy J. Identifying the ischaemic penumbra using pH-weighted magnetic resonance imaging. Brain 2015; 138(1): 36–42.
15. Jin T, Wang P, Zong X, Kim S-G. Magnetic resonance imaging of the Amine Proton EXchange (APEX) dependent contrast. Neuroimage 2012; 16(2): 1218–1227.
16. Cai K, Haris M, Singh A, Kogan F, Greenberg JH, Hariharan H, Detre JA, Reddy R. Magnetic resonance imaging of glutamate. Nat Med 2012; 18(2): 302–306.
17. Xu J, Zaiss M, Zu Z, Li H, Xie J, Gochberg DF, Bachert P, Gore JC. On the origins of chemical exchange saturation transfer (CEST) contrast in tumors at 9.4 T. NMR Biomed 2014; 27(4): 406–416.
18. Desmond KL, Moosvi F, Stanisz GJ. Mapping of amide, amine, and aliphatic peaks in the CEST spectra of murine xenografts at 7 T. Magn Reson Med 2014; 71(5): 1841–1853.

19. Chen LQ, Howison CM, Jeffery JJ, Robey IF, Kuo PH, Pagel MD. Evaluations of extracellular pH within in vivo tumors using acidoCEST MRI. Magn Reson Med 2014; 72(5): 1408–1417.
20. Chan KWY, Yu T, Qiao Y, Liu Q, Yang M, Patel H, Liu G, Kinzler KW, Vogelstein B, Bulte JWM, van Zijl PCM, Hanes J, Zhou S, McMahon MT. A diaCEST MRI approach for monitoring liposomal accumulation in tumors. J Control Release 2014; 180(0): 51–59.
21. Sagiyama K, Mashimo T, Togao O, Vemireddy V, Hatanpaa KJ, Maher EA, Mickey BE, Pan E, Sherry AD, Bachoo RM, Takahashi M. In vivo chemical exchange saturation transfer imaging allows early detection of a therapeutic response in glioblastoma. Proc Natl Acad Sci U S A 2014; 111(12): 4542–4547.
22. Haris M, Singh A, Mohammed I, Ittyerah R, Nath K, Nanga RPR, Debrosse C, Kogan F, Cai K, Poptani H, Reddy D, Hariharan H, Reddy R. In vivo magnetic resonance imaging of tumor protease activity. Sci Rep 2014; 4: 6081.
23. Jia G, Abaza R, Williams JD, Zynger DL, Zhou J, Shah ZK, Patel M, Sammet S, Wei L, Bahnson RR, Knopp MV. Amide proton transfer MR imaging of prostate cancer: a preliminary study. J Magn Reson Imaging 2011; 33(3): 647–654.
24. Cai K, Singh A, Poptani H, Li W, Yang S, Lu Y, Hariharan H, Zhou XJ, Reddy R. CEST signal at 2 ppm (CEST@2ppm) from *Z*-spectral fitting correlates with creatine distribution in brain tumor. NMR Biomed 2015; 28(1): 1–8.
25. Davis KA, Nanga RPR, Das S, Chen SH, Hadar PN, Pollard JR, Lucas TH, Shinohara RT, Litt B, Hariharan H, Elliott MA, Detre JA, Reddy R. Glutamate imaging (GluCEST) lateralizes epileptic foci in nonlesional temporal lobe epilepsy. Sci Transl Med 2015; 7(309): 309ra161–309ra161.
26. Sun PZ, van Zijl PCM, Zhou J. Optimization of the irradiation power in chemical exchange dependent saturation transfer experiments. J Magn Reson 2005; 175(2): 193–200.
27. McMahon M, Gilad A, Zhou J, Sun PZ, Bulte J, van Zijl PC. Quantifying exchange rates in chemical exchange saturation transfer agents using the saturation time and saturation power dependencies of the magnetization transfer effect on the magnetic resonance imaging signal (QUEST and QUESP): pH calibration for poly-L-lysine and a starburst dendrimer. Magn Reson Med 2006; 55(4): 836–847.
28. Sun PZ, Farrar CT, Sorensen AG. Correction for artifacts induced by B_0 and B_1 field inhomogeneities in pH-sensitive chemical exchange saturation transfer (CEST) imaging. Magn Reson Med 2007; 58(6): 1207–1215.
29. Sun PZ, Sorensen AG. Imaging pH using the chemical exchange saturation transfer (CEST) MRI: correction of concomitant RF irradiation effects to quantify CEST MRI for chemical exchange rate and pH. Magn Reson Med 2008; 60(2): 390–397.
30. Dixon TW, Ren J, Lubag A, Ratnakar J, Vinogradov E, Hancu I, Lenkinski RE, Sherry AD. A concentration-independent method to measure exchange rates in PARACEST agents. Magn Reson Med 2010; 63(3): 625–632.
31. Sun PZ, Wang Y, Xiao G, Wu R. Simultaneous experimental determination of labile proton fraction ratio and exchange rate with irradiation radio frequency power-dependent quantitative CEST MRI analysis. Contrast Media Mol Imaging 2013; 8(3): 246–251.
32. Sun PZ, Wang Y, Dai Z, Xiao G, Wu R. Quantitative chemical exchange saturation transfer (qCEST) MRI – RF spillover effect-corrected omega plot for simultaneous determination of labile proton fraction ratio and exchange rate. Contrast Media Mol Imaging 2014; 9(4): 268–275.
33. Longo DL, Sun PZ, Consolino L, Michelotti FC, Uggeri F, Aime S. A general MRI-CEST ratiometric approach for pH imaging: demonstration of *in vivo* pH mapping with iobitridol. J Am Chem Soc 2014; 136(41): 14333–14336.
34. Sun PZ. Simultaneous determination of labile proton concentration and exchange rate utilizing optimal RF power: radio frequency power (RFP) dependence of chemical exchange saturation transfer (CEST) MRI. J Magn Reson 2010; 202(2): 155–161.
35. Zu Z, Janve VA, Li K, Does MD, Gore JC, Gochberg DF. Multi-angle ratiometric approach to measure chemical exchange in amide proton transfer imaging. Magn Reson Med 2012; 68(3): 711–719.
36. Sun PZ, Xiao G, Zhou IY, Guo Y, Wu R. A method for accurate pH mapping with chemical exchange saturation transfer (CEST) MRI. Contrast Media Mol Imaging 2016; 11(3): 195–202.
37. Rerich E, Zaiss M, Korzowski A, Ladd ME, Bachert P. Relaxation-compensated CEST-MRI at 7 T for mapping of creatine content and pH – preliminary application in human muscle tissue in vivo. NMR Biomed 2015; 28(11): 1402–1412.
38. Liu G, Song X, Chan KWY, McMahon MT. Nuts and bolts of chemical exchange saturation transfer MRI. NMR Biomed 2013; 26(7): 810–828.
39. Kim J, Wu Y, Guo Y, Zheng H, Sun PZ. A review of optimization and quantification techniques for chemical exchange saturation transfer MRI toward sensitive in vivo imaging. Contrast Media Mol Imaging 2015; 10(3): 163–178.
40. Zaiss M, Bachert P. Chemical exchange saturation transfer (CEST) and MR *Z*-spectroscopy *in vivo*: a review of theoretical approaches and methods. Phys Med Biol 2013; 58(22): 221–269.
41. Sun PZ, Zhou J, Huang J, van Zijl P. Simplified quantitative description of amide proton transfer (APT) imaging during acute ischemia. Magn Reson Med 2007; 57(2): 405–410.
42. Shah T, Lu L, Dell KM, Pagel MD, Griswold MA, Flask CA. CEST-FISP: a novel technique for rapid chemical exchange saturation transfer MRI at 7 T. Magn Reson Med 2011; 65(2): 432–437.
43. Sun PZ, Wang Y, Lu J. Sensitivity-enhanced chemical exchange saturation transfer (CEST) MRI with least squares optimization of Carr Purcell Meiboom Gill multi-echo echo planar imaging. Contrast Media Mol Imaging 2014; 9(2): 177–181.
44. Sun PZ, Cheung JS, Wang E, Benner T, Sorensen AG. Fast multi-slice pH-weighted chemical exchange saturation transfer (CEST) MRI with unevenly segmented RF irradiation. Magn Reson Med 2011; 65(2): 588–594.
45. Song X, Gilad AA, Joel S, Liu G, Bar-Shir A, Liang Y, Gorelik M, Pekar JJ, van Zijl PCM, Bulte JWM, McMahon MT. CEST phase mapping using a length and offset varied saturation (LOVARS) scheme. Magn Reson Med 2012; 68(4): 1074–1086.
46. Sun PZ, Lu J, Wu Y, Xiao G, Wu R. Evaluation of the dependence of CEST-EPI measurement on repetition time, RF irradiation duty cycle and imaging flip angle for enhanced pH sensitivity. Phys Med Biol 2013; 58: N229–N240.
47. Zhou J, Blakeley JO, Hua J, Kim M, Laterra J, Pomper MG, van Zijl PCM. Practical data acquisition method for human brain tumor amide proton transfer (APT) imaging. Magn Reson Med 2008; 60(4): 842–849.
48. Sun PZ, Benner T, Copen WA, Sorensen AG. Early experience of translating pH-weighted MRI to image human subjects at 3 Tesla. Stroke 2010; 41(10 Suppl 1): S147–S151.
49. Ernst RR, Anderson WA. Application of Fourier transform spectroscopy to magnetic resonance. Rev Sci Instrum 1966; 37(1): 93–102.
50. Jin T, Autio J, Obata T, Kim S-G. Spin-locking versus chemical exchange saturation transfer MRI for investigating chemical exchange process between water and labile metabolite protons. Magn Reson Med 2011; 65(5): 1448–1460.
51. Murase K. Behavior of the magnetization in spin-locking magnetic resonance imaging using numerical solutions to the time-dependent Bloch equations. Phys Med Biol 2012; 57(23): 481–492.
52. Zaiss M, Bachert P. Exchange-dependent relaxation in the rotating frame for slow and intermediate exchange – modeling off-resonant spin-lock and chemical exchange saturation transfer. NMR Biomed 2013; 26(5): 507–518.
53. Zaiss M, Xu J, Goerke S, Khan IS, Singer RJ, Gore JC, Gochberg DF, Bachert P. Inverse *Z*-spectrum analysis for spillover-, MT-, and T_1-corrected steady-state pulsed CEST-MRI – application to pH-weighted MRI of acute stroke. NMR Biomed 2014; 27(3): 240–252.
54. Trott O, Palmer AG. R1rho relaxation outside of the fast-exchange limit. J Magn Reson 2002; 154(1): 157–160.
55. Lee J-S, Xia D, Jerschow A, Regatte RR. *In vitro* study of endogenous CEST agents at 3 T and 7 T. Contrast Media Mol Imaging 2016; 11(1): 4–14.
56. Goerke S, Zaiss M, Bachert P. Characterization of creatine guanidinium proton exchange by water-exchange (WEX) spectroscopy for absolute-pH CEST imaging *in vitro*. NMR Biomed 2014; 27 (5): 507–518.
57. Zhao X, Wen Z, Huang F, Lu S, Wang X, Hu S, Zu D, Zhou J. Saturation power dependence of amide proton transfer image contrasts in human brain tumors and strokes at 3 T. Magn Reson Med 2011; 66(4): 1033–1041.
58. Singh A, Haris M, Cai K, Kassey VB, Kogan F, Reddy D, Hariharan H, Reddy R. Chemical exchange saturation transfer magnetic resonance imaging of human knee cartilage at 3 T and 7 T. Magn Reson Med 2012; 68(2): 588–594.

59. Lee J-S, Parasoglou P, Xia D, Jerschow A, Regatte RR. Uniform magnetization transfer in chemical exchange saturation transfer magnetic resonance imaging. Sci Rep 2013; 3: 1707.
60. Dula AN, Arlinghaus LR, Dortch RD, Dewey BE, Whisenant JG, Ayers GD, Yankeelov TE, Smith SA. Amide proton transfer imaging of the breast at 3 T: establishing reproducibility and possible feasibility assessing chemotherapy response. Magn Reson Med 2013; 70(1): 216–224.
61. Stanisz GJ, Odrobina EE, Pun J, Escaravage M, Graham SJ, Bronskill MJ, Henkelman RM. T1, T2 relaxation and magnetization transfer in tissue at 3 T. Magn Reson Med 2005; 54(3): 507–512.
62. Sun PZ, Wang E, Cheung JS, Zhang X, Benner T, Sorensen AG. Simulation and optimization of pulsed radio frequency (RF) irradiation scheme for chemical exchange saturation transfer (CEST) MRI – demonstration of pH-weighted pulsed-amide proton CEST MRI in an animal model of acute cerebral ischemia. Magn Reson Med 2011; 66(4): 1042–1048.
63. Zu Z, Li K, Janve VA, Does MD, Gochberg DF. Optimizing pulsed-chemical exchange saturation transfer imaging sequences. Magn Reson Med 2011; 66(4): 1100–1108.
64. Meissner J-E, Goerke S, Rerich E, Klika KD, Radbruch A, Ladd ME, Bachert P, Zaiss M. Quantitative pulsed CEST-MRI using Ω-plots. NMR Biomed 2015; 28(10): 1196–1208.
65. Woessner DE, Zhang S, Merritt ME, Sherry AD. Numerical solution of the Bloch equations provides insights into the optimum design of PARACEST agents for MRI. Magn Reson Med 2005; 53(4): 790–799.

APPENDIX

A.1. Steady state non-thermal equilibrium CEST effect solution

The control signal without RF saturation can be shown to be

$$S_0(TR) = \frac{1 - e^{-TR/T_{1w}}}{1 - \cos(FA)e^{-TR/T_{1w}}}\sin(FA). \quad (A1.1)$$

For the saturated scan, the *Z*-magnetization at the beginning of the sequence ($t = 0$) after the previous saturation is given by

$$I_{sat}(0) = I_{sat}(TR)\cos(FA). \quad (A1.2a)$$

The *Z*-magnetization evolves towards its equilibrium state following standard relaxation recovery, and we have

$$I_{sat}(T_r) = I_{sat}(TR)\cos(FA)e^{-T_r/T_{1w}} + \left(1 - e^{-T_r/T_{1w}}\right). \quad (A1.2b)$$

The spin signal evolution following the RF saturation can be described by the spin locking theorem, and we have

$$\begin{aligned} I_{sat}(TR) &= I_{sat}(T_r)e^{-R_{1\rho}T_s} + \frac{R_{1w}\cos^2\theta}{R_{1\rho}}\left(1 - e^{-R_{1\rho}T_s}\right) \\ &= \left(I_{sat}(TR)\cos(FA)e^{-T_r/T_{1w}} + \left(1 - e^{-T_r/T_{1w}}\right)\right)e^{-R_{1\rho}T_s} \\ &\quad + \frac{R_{1w}\cos^2\theta}{R_{1\rho}}\left(1 - e^{-R_{1\rho}T_s}\right). \end{aligned} \quad (A1.2c)$$

The steady state signal can be solved as

$$I_{sat}(TR) = \frac{\left(1 - e^{-T_r/T_{1w}}\right)e^{-R_{1\rho}T_s} + \frac{R_{1w}\cos^2\theta}{R_{1\rho}}\left(1 - e^{-R_{1\rho}T_s}\right)}{1 - \cos(FA)e^{-T_r/T_{1w}}e^{-R_{1\rho}T_s}}. \quad (A1.3)$$

Hence, the detectable signal is the sine projection of magnetization $I_{sat}(TR)$.

$$\begin{aligned} S_{sat}(TR) &= I_{sat}(TR)\sin(FA) \\ &= \frac{\left(1 - e^{-T_r/T_{1w}}\right)e^{-R_{1\rho}T_s} + \frac{R_{1w}\cos^2\theta}{R_{1\rho}}\left(1 - e^{-R_{1\rho}T_s}\right)}{1 - \cos(FA)e^{-T_r/T_{1w}}e^{-R_{1\rho}T_s}}\sin(FA). \end{aligned} \quad (A1.4)$$

CESTR and $CESTR_{ind}$ can be calculated as $CESTR = \frac{S_{ref} - S_{lab}}{S_0}$ and $CESTR_{ind} = \frac{S_0}{S_{lab}} - \frac{S_0}{S_{ref}}$, respectively.

A.2. CEST MRI SNR derivation

(a) For routine CESTR, the standard deviation can be obtained as

$$\begin{aligned} \sigma^2_{CESTR} &= \left(\frac{\partial CESTR}{\partial S_{ref}}\right)^2\sigma^2_{ref} + \left(\frac{\partial CESTR}{\partial S_{lab}}\right)^2\sigma^2_{label} + \left(\frac{\partial CESTR}{\partial S_0}\right)^2\sigma^2_0 \\ &= \frac{\sigma^2_{ref}}{S_0^2} + \frac{\sigma^2_{label}}{S_0^2} + \left(\frac{S_{ref} - S_{label}}{S_0^2}\right)^2\sigma^2_0 \\ &= \left(2 + CESTR^2\right)\frac{\sigma^2}{S_0^2}. \end{aligned} \quad (A2.1)$$

If the noise level remains stable and dominated by the thermal noise, the noise terms can be treated as the same for all images. The SNR for the routine CESTR can be shown to be

$$SNR_{CESTR} = \frac{CESTR}{\sigma_{CESTR}} = \frac{CESTR}{\sqrt{2 + CESTR^2}}SNR_{S_0(TR,FA)}. \quad (A2.2)$$

(b) For the inverse CEST asymmetry of $CESTR_{ind}$, we have

$$CESTR_{ind} = \frac{S_0}{S_{lab}} - \frac{S_0}{S_{ref}} = CESTR\left(\frac{S_0^2}{S_{ref}S_{label}}\right). \quad (A2.3)$$

The standard deviation of $CESTR_{ind}$ can be obtained as

$$\begin{aligned} \sigma^2_{CESTR_{ind}} &\approx \left(\frac{\partial CESTR_{ind}}{\partial S_{ref}}\right)^2\sigma^2_{ref} + \left(\frac{\partial CESTR_{ind}}{\partial S_{label}}\right)^2\sigma^2_{label} + \left(\frac{\partial CESTR_{ind}}{\partial S_0}\right)^2\sigma^2_0 \\ &= \left[\left(\frac{S_0^2}{S_{ref}^2}\right)^2 + \left(\frac{S_0^2}{S_{label}^2}\right)^2 + \left(\frac{S_0}{S_{label}} - \frac{S_0}{S_{ref}}\right)^2\right]\frac{\sigma^2_0}{S_0^2}. \end{aligned} \quad (A2.4)$$

Its SNR can be shown to be

$$\mathrm{SNR}_{\mathrm{CESTR}_{\mathrm{ind}}} = \frac{\mathrm{CESTR}_{\mathrm{ind}}}{\sqrt{\frac{1}{S_0^2}\left[\left(\frac{S_0^2}{S_{\mathrm{ref}}^2}\right)^2 + \left(\frac{S_0^2}{S_{\mathrm{label}}^2}\right)^2\right]\sigma^2 + \mathrm{CESTR}_{\mathrm{ind}}^2\frac{\sigma^2}{S_0^2}}} = \frac{\mathrm{CESTR}_{\mathrm{ind}}}{\sqrt{\frac{1}{S_0^2}\left[2\frac{S_0^2}{S_{\mathrm{ref}}^2}\frac{S_0^2}{S_{\mathrm{label}}^2} + \left(\frac{S_0^2}{S_{\mathrm{ref}}^2} - \frac{S_0^2}{S_{\mathrm{label}}^2}\right)^2\right]\sigma^2 + \mathrm{CESTR}_{\mathrm{ind}}^2\frac{\sigma^2}{S_0^2}}}. \quad \text{(A2.5)}$$

This can be simplified as

$$\mathrm{SNR}_{\mathrm{CESTR}_{\mathrm{ind}}} = \frac{\mathrm{CESTR}_{\mathrm{ind}}}{\sqrt{\left[2\frac{S_0^2}{S_{\mathrm{ref}}^2}\frac{S_0^2}{S_{\mathrm{label}}^2} + \left(\left(\frac{S_0}{S_{\mathrm{ref}}} - \frac{S_0}{S_{\mathrm{label}}}\right)\left(\frac{S_0}{S_{\mathrm{ref}}} + \frac{S_0}{S_{\mathrm{label}}}\right)\right)^2\right] + \mathrm{CESTR}_{\mathrm{ind}}^2}}\mathrm{SNR}_{S_0(TR,\mathrm{FA})} = \frac{\mathrm{CESTR}_{\mathrm{ind}}}{\sqrt{\left[2\left(\frac{S_0^2}{S_{\mathrm{ref}}S_{\mathrm{label}}}\right)^2 + \left(\mathrm{CESTR}_{\mathrm{ind}}\left(\frac{S_0}{S_{\mathrm{ref}}} + \frac{S_0}{S_{\mathrm{label}}}\right)\right)^2\right] + \mathrm{CESTR}_{\mathrm{ind}}^2}}\mathrm{SNR}_{S_0(TR,\mathrm{FA})}. \quad \text{(A2.6)}$$

Because $\mathrm{CESTR}_{\mathrm{ind}} = \mathrm{CESTR}\left(\frac{S_0^2}{S_{\mathrm{ref}}S_{\mathrm{label}}}\right)$, $SNR_{CESTR_{ind}}$ can be further expressed as

$$\mathrm{SNR}_{\mathrm{CESTR}_{\mathrm{ind}}} = \frac{\mathrm{CESTR}^2}{\sqrt{2 + \mathrm{CESTR}^2\left(1 + \left(\frac{S_0}{S_{\mathrm{ref}}} + \frac{S_0}{S_{\mathrm{label}}}\right)^2\right)}}\mathrm{SNR}_{S_0(TR,\mathrm{FA})}. \quad \text{(A2.7)}$$

For small CEST effect (i.e., $\mathrm{CESTR}^2 \ll 1$), we have $SNR_{CESTR_{ind}} \approx SNR_{CESTR}$.

(c) For the RF-power based ratiometric analysis (i.e., $\mathrm{PRCESTR} = \mathrm{CESTR}(B_{1a})/\mathrm{CESTR}(B_{1b})$), we have

$$\sigma_{\mathrm{PRCESTR}}^2 \approx \left(\frac{\partial \mathrm{PRCESTR}}{\partial \mathrm{CESTR}(B_{1a})}\right)^2\sigma_{\mathrm{CESTR}(B_{1a})}^2 + \left(\frac{\partial \mathrm{PRCESTR}}{\partial \mathrm{CESTR}(B_{1b})}\right)^2\sigma_{\mathrm{CESTR}(B_{1b})}^2 = \frac{1}{\mathrm{CESTR}^2(B_{1b})}\sigma_{\mathrm{CESTR}(B_{1a})}^2 + \frac{\mathrm{CESTR}^2(B_{1a})}{\mathrm{CESTR}^4(B_{1b})}\sigma_{\mathrm{CESTR}(B_{1b})}^2 = \frac{\mathrm{CESTR}^2(B_{1a})}{\mathrm{CESTR}^2(B_{1b})}\left(\frac{1}{\mathrm{SNR}_{\mathrm{CESTR}(B_{1a})}^2} + \frac{1}{\mathrm{SNR}_{\mathrm{CESTR}(B_{1b})}^2}\right). \quad \text{(A2.8)}$$

Hence its SNR can be shown to be

$$\mathrm{SNR}_{\mathrm{PRCESTR}} = \frac{\frac{\mathrm{CESTR}(B_{1a})}{\mathrm{CESTR}(B_{1b})}}{\sqrt{\frac{1}{\mathrm{CESTR}^2(B_{1b})}\sigma_{\mathrm{CESTR}(B_{1a})}^2 + \frac{\mathrm{CESTR}^2(B_{1a})}{\mathrm{CESTR}^4(B_{1b})}\sigma_{\mathrm{CESTR}(B_{1b})}^2}} = \frac{\mathrm{CESTR}(B_{1a})\mathrm{CESTR}(B_{1b})}{\sqrt{\mathrm{CESTR}^2(B_{1b})\sigma_{\mathrm{CESTR}(B_{1a})}^2 + \mathrm{CESTR}^2(B_{1a})\sigma_{\mathrm{CESTR}(B_{1b})}^2}} == \frac{\mathrm{SNR}_{\mathrm{CESTR}(B_{1a})}\mathrm{SNR}_{\mathrm{CESTR}(B_{1b})}}{\sqrt{\mathrm{SNR}_{\mathrm{CESTR}(B_{1a})}^2 + \mathrm{SNR}_{\mathrm{CESTR}(B_{1st})}^2}}. \quad \text{(A2.9)}$$

The same formula is applicable to RF-power based ratiometric analysis of inverse CEST asymmetry (PRICESTR).

A.3. CEST MRI CNR derivation

The relationship between the CNR and SNR of any two signals can be generally described as the following. We denote the contrast as $C = S(a) - S(b)$, where $S(a)$ and $S(b)$ represent two CEST effects. We have

$$\sigma_C^2 \approx \left(\frac{\partial C}{\partial S(a)}\right)^2\sigma_{S(a)}^2 + \left(\frac{\partial C}{\partial S(b)}\right)^2\sigma_{S(b)}^2 = \sigma_{S(a)}^2 + \sigma_{S(b)}^2. \quad \text{(A3.1)}$$

The CNR can be shown to be

$$\mathrm{CNR} = \frac{|S(a) - S(b)|}{\sqrt{\sigma_{S(a)}^2 + \sigma_{S(b)}^2}} = \frac{|S(a) - S(b)|}{\sqrt{\left(\frac{S(a)}{\mathrm{SNR}_{S(a)}}\right)^2 + \left(\frac{S(b)}{\mathrm{SNR}_{S(b)}}\right)^2}} = \frac{|S(a) - S(b)|}{\sqrt{\left(S(a)\mathrm{SNR}_{S(b)}\right)^2 + \left(S(b)\mathrm{SNR}_{S(a)}\right)^2}}\mathrm{SNR}_{S(a)}\mathrm{SNR}_{S(b)}. \quad \text{(A3.2)}$$